JMEPEG (2008) 17:928–935
DOI: 10.1007/s11665-008-9241-5

1059-9495/$19.00

Microstructure and Phase Composition of a Low-Power YAG Laser-MAG Welded Stainless Steel Joint

R. S. Huang, L. Kang, and X. Ma

(Submitted April 10, 2007; in revised form March 8, 2008)

This article presents multipass hybrid welding of austenitic stainless steel (ASS) structure by using the low-power Nd:YAG laser-metal active gas (MAG) arc hybrid welding method. The purpose of this work is to investigate and qualify the effects of multipass hybrid welding of ASS structure on the microstructure, phase composition, weld postheat influence, and weld bead (WB) precipitated phase. The results demonstrated that sound welded joints without any solidification and shrinkage defects could be obtained after welding. The top and the bottom portions of the workpieces were joined completely. At room temperature, the microstructures of different regions in WB were different and the WB microstructures were composed of columnar γ-austenite and δ-ferrite phases. The fraction of δ-ferrite decreased from 20% to 10%, and its morphology changed orderly from lath, skeleton, vermicular to reticular with an increase in the number of welding cycles. Because of the influence of postweld heat, the weld metal phase chemistry at 3 mm distance from the top of the WB surface underwent a notable modification that corresponded to an evolution of the partition coefficients toward the parent metal values. This indicated corrosion resistance of the microstructure is equivalent to that of the parent metal.

Keywords low-power laser, microstructure, partition coefficient, stainless steel, YAG laser-MAG hybrid welding

1. Introduction

The laser-tungsten inert gas (TIG) arc hybrid welding process was first presented by W. M. Steen and M. Eboo in the late 1970s (Ref 1). Compared with the laser welding and conventional arc welding, the laser-arc hybrid welding avoids the disadvantage of individual process and has its own particular advantages, such as increased welding penetration, improved welding efficiency, reduced welding cost, the ability to bridge large gaps, etc. Therefore, the hybrid welding technologies have become a focus in international welding area in the last 10 years (Ref 2-6). Especially in recent years, with the industrial development of shipbuilding and car manufacturing, where deep weld penetration and welding of thick steel plates and aluminum alloys may be needed, investigations of laser-metal inert gas\metal active gas (MIG\MAG) hybrid welding have became more attractive and have already been carried out for practical application in many industrial fields (Ref 7, 8).

R. S. Huang, The State Key Laboratory of Materials Modification and School of Materials Science and Engineering, Dalian University of Technology, Dalian 116024, People's Republic of China; and **L. Kang and X. Ma**, The Ministry of Education Research Center of Photo-Electricity Function Materials & School of Materials Science and Engineering, Chang Chun University of Science and Technology, Chang Chun 130022, People's Republic of China. Contact e-mail: huangrs8@163.com.

However, in recent years, investigations of laser-arc hybrid welding have focused on high-power laser-MIG hybrid welding, which would result in some disadvantages to the practical industrial applications, such as low efficiency and economy, high welding cost, and high energy consumption (Ref 7). To reduce the energy consumption and other disadvantages of high-power laser-arc hybrid welding process, recently, attention has been paid to low-power laser-arc-hybrid welding process. With regard to low-power laser-arc hybrid welding technology, most of the papers have investigated the effect of welding parameters, but only a few papers have investigated the physical phenomenon and mechanism. Shinn et al. (Ref 9) reported that it was possible to ensure the arc burning steadily having a laser power of 200 W when the dimension of laser-heated spot was 0.6 mm. Hu et al. (Ref 10) discovered in YAG laser-TIG arc hybrid welding process with 500 W laser that the stabilization of welding arc and the molten efficiency increased compared with that in TIG welding process. Earlier research on low-power YAG laser-arc hybrid welding process by the group of present authors found that there was a distinct increase in both the weld penetration depth and the weld speed compared with either the laser process or the TIG process alone (Ref 11-16).

Austenitic stainless steels (ASS), which have relatively high mechanical strength and excellent fabrication properties and low cost, especially the combination of high yield strength and toughness coupled with excellent corrosion resistance in the temperature range from 223 K to 523 K, are commonly used for construction in marine, power generation, and chemical industries. With respect to the properties of ASS weldment, many research studies have been carried out for many years (Ref 17-20). ASS are weldable by conventional welding processes in spite of their sophisticated metallurgy, but a lot of problems arise from the crystal boundary corrosion, stress corrosion, hot cracking of welded joint, etc., and these

facts are related to the microstructures of ASS weld bead (WB) (Ref 21, 22). In this article, the optimal welding parameters, the precipitated phase of WB, the morphology and fraction of δ-ferrite as well as postheat influence on microstructures of WB are investigated by using the low-power YAG laser-MAG arc hybrid welding method. The goal is to supply a basis for solving a lot of problems of ASS-welded joints and to enable the practical application of this energy-saving hybrid welding technology.

2. Experimental Procedure

Low-power pulsed YAG laser (LWS-500YAG) with the maximum power of 500 W was used together with a MIG/MAG welding equipment (YD-350AG1). The sketch of setup in hybrid welding process is shown in Fig. 1.

In the experiment, the workpiece of AISI 304 stainless steel was used, which was solution treated at 1323 K. The structure is shown in Fig. 2. Before welding, the surface of workpiece and the two sides of grooves were cleaned with acetone and scratch brushed to maintain consistent surfaces conditions. A welding wire of MIG-308 (AWS, A5.9 ER308) with a diameter of 1.2 mm was used. The shield gas composed of Ar (80%) and CO_2 (20%) was spurted out from the nozzle of MAG welding torch. The sequence of multipass welding is shown in Fig. 3.

Table 1 shows the welding parameters. When one WB was finished, the shield gas blow off from the blowtorch was sustained for 10-30 s. The gas feeding rate is not changed in the welding process. The welding parameters (e.g. welding current, welding voltage, and welding speed) of each WB is different from root to top. The slag is removed by grinding wheel and the oxide on the surface of WB is scratch brushed, respectively, after the welding of each WB.

After welding, samples, which were transverse to WB, were cut from the weldment and prepared for metallographic analyses by grinding, polishing, and etching. The microstructures of the welded joint were analyzed by optical and scanning electron microscopy, and microchemical composition of the phases and the precipitated phase in WB was determined by energy dispersive spectroscopy (EDS) fitted to the scanning electron microscope (SEM). Quantitative image analysis was

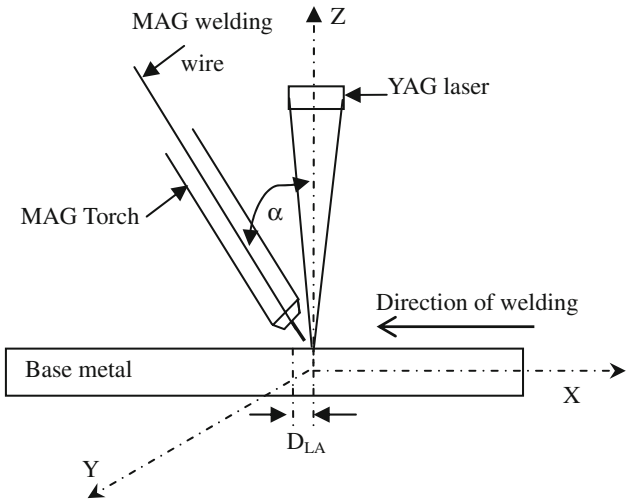

Fig. 1 Setup of hybrid welding

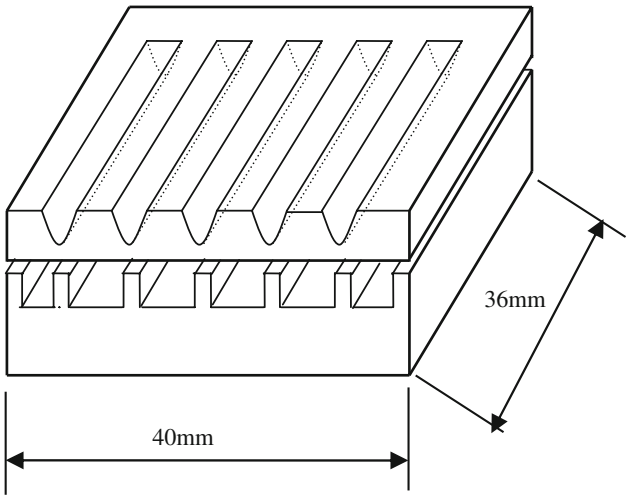

Fig. 2 Diagrammatic sketch of workpiece

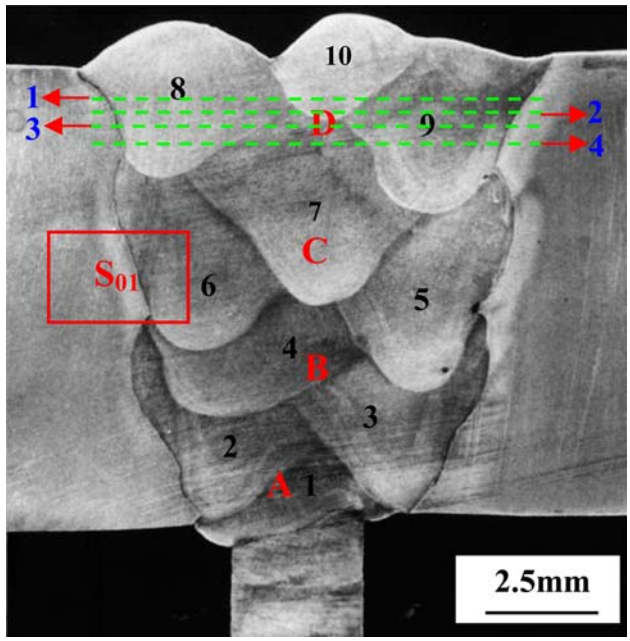

Fig. 3 Cross-sectional view of the weld joint

Table 1 Experimental conditions

Welding parameters	Values
Laser power, pulsed, *P*, W	360
Focal length, *f*, mm	121
Defocusing amount, Δ*z*, mm	0
MAG current, pulsed, *I*, A	170-210
MAG voltage, *U*, V	20-30
Wire feed rate, m min^{-1}	10.2
Gas feeding rate, *L* min^{-1}	15
Welding speed, *v*, m min^{-1}	0.6-1
Distance between laser and arc, D_{LA}, mm	+0.5
Angle between laser and nozzle, α, degree	45

performed on optical micrographs taken from the WB to calculate the ferrite volume fractions. The phase volume fraction was determined by the manual point count method on micrographs taken at 500× magnifications, in accordance to ASTM E562-95 standard.

3. Results and Discussion

3.1 Microstructures

Figure 3 illustrates the cross-sectional view of welded joint. It shows that sound joint without any solidification and shrinkage defects is obtained, the weld zone of each joint is fused well, the top and the bottom portions of workpieces are joined completely, and the weld surface is smooth. The fusion zone (FZ) in the S_{01} rectangular area of Fig. 3 is magnified for further analysis as shown in Fig. 4(a). For crystal grain size, the crystal grains in heat affected zone (HAZ) are coarse and lamellar, while those in the WB are small and columnar.

In hybrid welding, the arc can preheat workpiece surface before laser irradiation, and a shallow melting zone which reduces the reflectivity of workpiece for the laser is formed. Consequently, the extra heat input enlarged the total molten weld pool volume surrounding the laser keyhole as indicated by the weld pool size. The enlarged weld pool enables the weld pool fluctuation to damp down and form a smooth WB surface. The extra heat input increased the melting energy (parent metal and filler wire) and the top and the bottom portions of workpieces were joined completely.

In multipass hybrid welding, the microstructures that form in hybrid welding differ from those in autogenous laser welding and arc welding. This is partly because of difference of cooling effect resulting from the multipass welding, and the increased heat input from additional arc power and the new heat produced by each welding bead which is input to the previous WB. This causes the microstructures of the previous WB and the surrounding area to grow with increased welding cycles. In the first welding process, the heat of the molten pool was transmitted mostly through unmelted parent metal. Because the brim of the molten pool was the first portion to cool down and solidify, nucleating particles of the new phase in the molten pool were supplied by unmelted parent metal particles during solidification. This resulted in a large number of columnar crystal grains generated in the brim of the molten pool in the WB root. During the second welding process, the molten metal was made up of the metal filler and the residual part of the 1st WB. The microstructures of the 1st WB had already grown, according to the pattern mentioned above and the crystal grains of the 2nd WB grew up sequentially. Formation of microstructures from 3rd to10th WB followed the same pattern. Owing to the slow cooling rate, small temperature gradient and quick crystal growth rate, which are related to the heat conductivity of ASS, the size of crystal grains in WB center and WB head

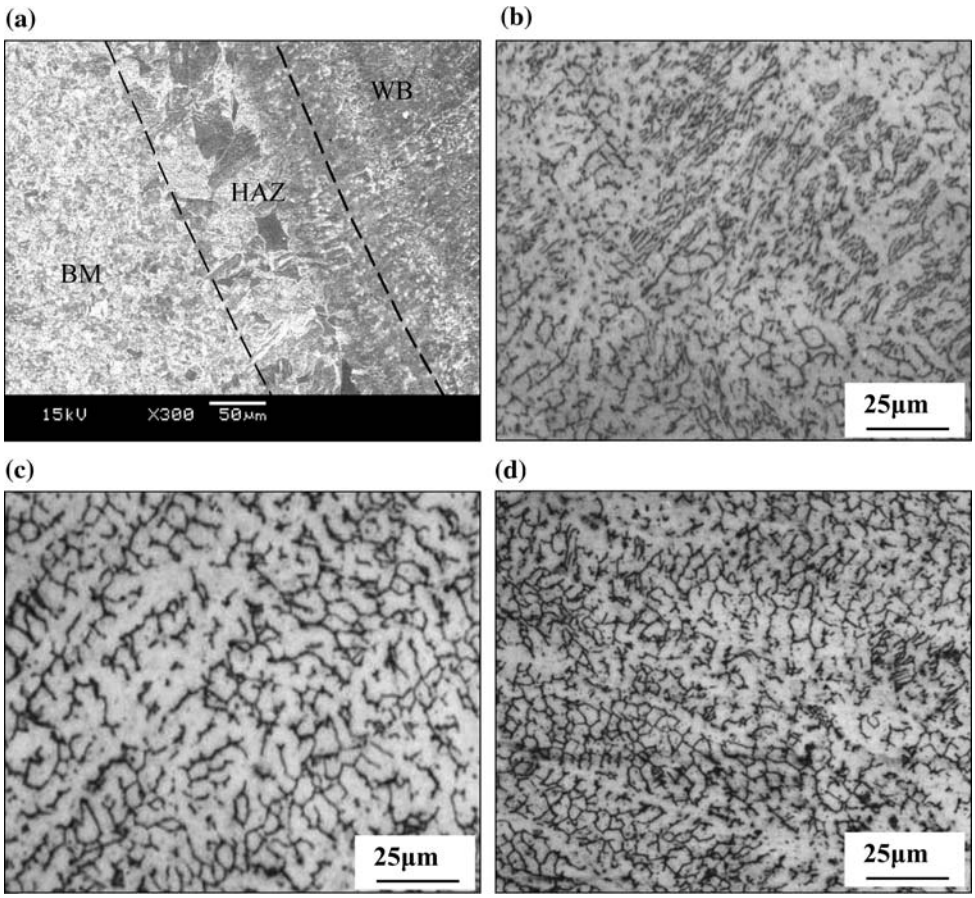

Fig. 4 Microstructures of different positions in WB. (a) Fusion zone at the S_{01} rectangular area of Fig. 3. (b) The head of WB at the D region of Fig. 3. (c) The center of WB at the C region of Fig. 3. (d) The root of WB at the A region of Fig. 3

increased compared with those in the WB root. In addition, previous WB grains would be recrystallized and it caused much larger grains to be produced during cooling and solidification process.

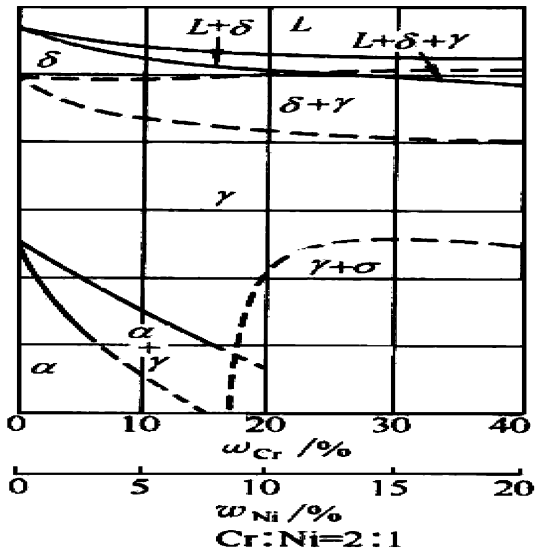

Fig. 5 Pseudo-binary diagram of Fe-Cr-Ni

3.2 Fraction and Morphology of δ-Ferrite Microstructure

In hybrid welding process, the welding speed is high, the heat input of molten metal per unit of meter decreases, and the duration of the molten metal in high temperature area is little. These factors cause the solidification rate of molten metal to change quickly. Consequently solidification rate plays an important role in alloying element microsegregation in the microstructure. In general, the higher the solidification rate, the finer the microstructure and second phase boundaries, and the lesser the microsegregation.

It has been reported that there are four possible different solidification modes for stainless steel welds: (1) fully austenitic, (2) primary austenitic, (3) primary ferritic, and (4) fully ferritic. Each solidification mode results in distinctive austenite and ferrite morphologies (Ref 23). The chemical compositions of the parent metal and the filler metal, as well as the weld thermal cycle, determine the WB microstructure of ASS weldment. Since nonequilibrium conditions were operative, when most of the ASS weld metals were produced in the present experiment, they solidified initially in the fully ferritic mode. As indicated by the modified pseudo-binary diagram of Fig. 5, for a Cr/Ni equivalent ratio of 2:1, ferrite is the only phase that forms directly from the liquid (Ref 22). Transformation of δ-ferrite to austenite subsequently occurs in the solid state, in the temperature range between 1573 and 1073 K. The weld metal microstructures are shown in Fig. 6(a-d). In the weld metal, δ-ferrite solidification involves an epitaxial growth

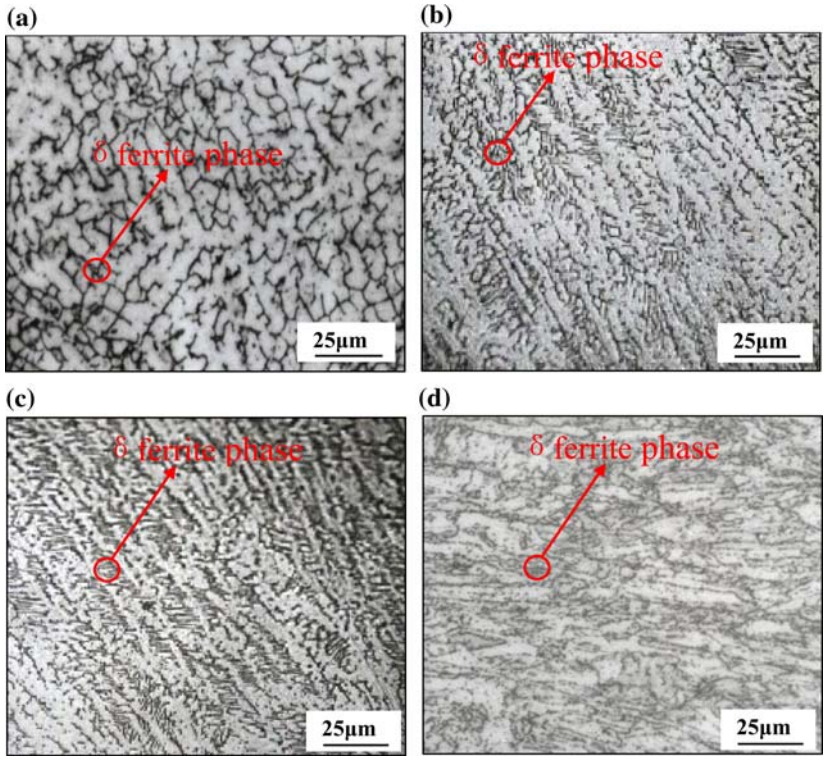

Fig. 6 The fraction and morphology of δ-ferrite at different WB positions. (a) The fraction of reticular δ-ferrite at D region of Fig. 3 is 10% and the component of each phase (wt.%). γ-austenite: Cr = 22.31, Ni = 6.78, Si = 0.73, Mo = 0.41; δ-ferrite: Cr = 23.47, Ni = 6.32, Si = 1.43, Mo = 0.24. (b) The fraction of vermicular δ-ferrite at C region of Fig. 3 is 15% and the component of each phase (wt.%). γ-austenite: Cr = 21.77, Ni = 7.07, Si = 1.26, Mo = 1.27; δ-ferrite: Cr = 22.87, Ni = 6.58, Si = 2.45, Mo = 0.72. (c) The fraction of skeleton δ-ferrite at B region of Fig. 3 is 18% and the component of each phase (wt.%). γ-austenite: Cr = 19.79, Ni = 8.01, Si = 0.81, Mo = 1.00; δ-ferrite: Cr = 20.76, Ni = 7.44, Si = 1.58, Mo = 0.82. (d) The fraction of lath δ-ferrite at A region of Fig. 3 is 20% and the component of each phase (wt.%). γ-austenite: Cr = 14.80, Ni = 4.67, Si = 0.25, Mo = 0.97; δ-ferrite: Cr = 15.77, Ni = 4.67, Si = 0.50, Mo = 0.52

from the molten parent metal boundary. The epitaxial and competitive nature of δ-ferrite grain in ASS welds promotes the formation of a coarse columnar austenite grain structure. It is observed from Fig. 6(a-d) that the fraction of δ-ferrite phase decreases from 20% to 10%, its morphology changes orderly from lath, skeleton, vermicular to reticular with an increase in welding cycles, and the fine precipitates appear in the ferrite phase. During cooling of the weld metals in the temperature range between 1573 and 1073 K, the austenite started to precipitate at the ferrite grain boundaries and at the weld metal surface due to higher free energy of these locations. The extent of this precipitation depends on the chemical composition and the cooling rate.

3.3 Postweld Heat Influence

As expected, the extent of modification of the WB metal was affected by postweld heat with welding cycles increasing in hybrid multipass welding process. In addition, different microstructure features were observed at different distances from the top of the WB. Figure 7 depicts a series of SEM micrographs observed in different WB regions (at 2, 3, 4, and 6 mm from the top of the WB surface) see from the 1st to the 4th line in Fig. 3). The modified weld metal structure featured an increasing amount of ferrite, which formed both at the coarse pre-existing austenite grain boundary and at the intragranular sites with higher free energy. Its morphology changes to granular and lath. In addition a fine precipitate appears in the austenite. More specifically, from Fig. 7, it is inferred that the partial decomposition of austenite took place by the growth of the ferrite phase, according to Widmanstätten-type mechanism, from original coarse grain boundaries and by the nucleation and/or growth of small precipitates inside the ferrite grains. Additional information on microstructure evolution due to postweld heat was gathered by careful measurement of element concentration in austenite and ferrite phases in different regions of the WB. The results of EDS microanalyses performed on austenite and ferrite islands which are in the parent metal and different positions of WB from top surface are summarized in Table 2. From the data, the partition coefficients of the different elements were calculated as the amount of each element in the ferrite phase with respect to that in the austenite phase ($\%el_\delta/\%el_\gamma$). The results obtained are graphically shown in Fig. 8. From the data given in Table 2 and the partition coefficients plotted in Fig. 8, it is evident that in the parent metal, elemental distribution between ferrite and austenite had well developed according to the high temperature equilibrium conditions established during the solution treatment at 1327 K. The values obtained for the partition coefficients are consistent with the data presented in the literature on similar steel grades (Ref 24). But in the rapidly cooled weld metals of WB root,

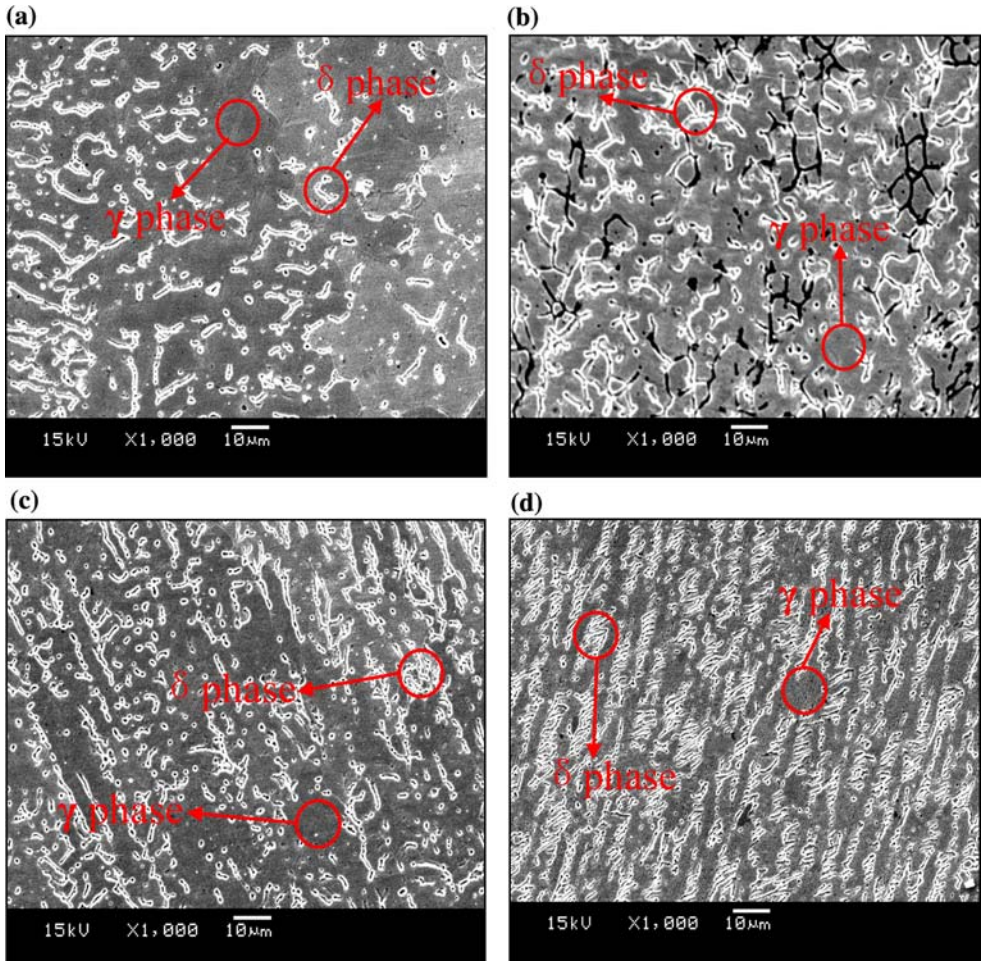

Fig. 7 Secondary electron view of different regions in welded structure at (a) 2 mm, (b) 3 mm, (c) 4 mm, and (d) 6 mm

Table 2 The element concentration in austenite and ferrite islands in the parent metal and in WB at different positions from top surface (wt.%)

	Phase	Cr	Ni	Si	Mn	Mo
Parent metal	δ-ferrite	18.79	8.01	1.53	1.25	0.54
	γ-austenite	17.9	11.9	1.25	1.47	0.47
2 mm from surface	δ-ferrite	22.31	6.78	0.73	1.66	0.42
	γ-austenite	21.89	7.89	0.63	1.65	0.36
3 mm from surface	δ-ferrite	22.24	6.95	0.65	1.35	0.37
	γ-austenite	21.48	8.48	0.53	1.52	0.31
4 mm from surface	δ-ferrite	23.36	6.96	1.22	1.64	0.30
	γ-austenite	23.12	7.65	1.15	1.66	0.28
5 mm from surface	δ-ferrite	23.47	6.32	1.43	1.72	0.25
	γ-austenite	22.79	7.02	1.35	1.54	0.25
6 mm from surface	δ-ferrite	19.78	7.66	1.07	1.12	0.25
	γ-austenite	19.77	7.74	1	1.13	0.24

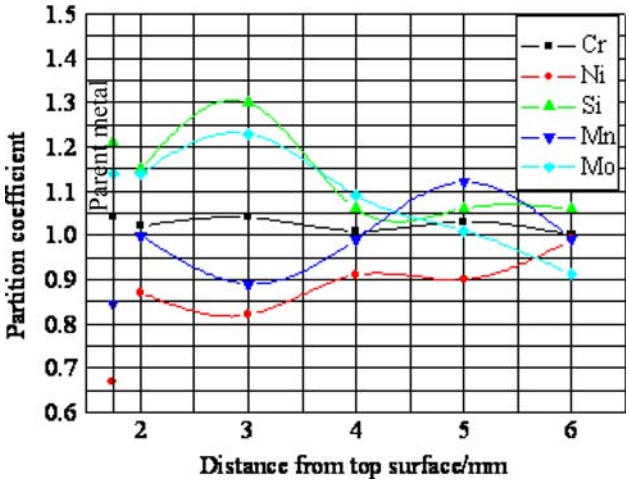

Fig. 8 Partition coefficients between ferrite and austenite in the weld metal at different distances from top surface and in the solution treated parent metal

no substantial partitioning between ferrite-stabilizing and austenite-stabilizing elements occurred. And because of the influence of postweld heat, the weld metal phase chemistry at 3 mm (the third line in Fig. 3) from the top of the WB surface underwent a notable modification that corresponded to an evolution of the partition coefficients toward the parent metal values.

3.4 The Precipitated Phase Analysis

Figure 9(a) shows the secondary electron image of WB root (the A regions in Fig. 3). It is seen that some blocks occur inside the grain and sometimes at the grain boundary. According to the Fe-Cr binary phase diagram, the σ phase (chemical compound of Fe-Cr) will appear from the δ-ferrite at low temperature (≈1093 K). During hybrid welding, the solidification process of the weld metal was a nonequilibrium process, and because the quickest cooling rate was in the root regions of WB, the σ phase could appear in the root regions of WB. The EDS analysis of Fig. 9(b) indicated that the white block contains up to 15.38 and 83.48 wt.% of Cr and Fe, respectively. So the white blocks are indicated as σ phase.

4. Discussion

The results of the present investigation confirm previous experimental works that revealed the advantages of low-power YAG-MAG Hybrid Welding process (Ref 13-17). After process optimization, defect-free weld joints with a controlled WB shape were produced. However, it was also shown that the balanced structures which were made up of austenite and ferrite were different in different areas of welded joint, due to the different cooling rate of different areas after solidification that prevented the transformation of part of the ferrite into austenite.

Microstructural analysis of the WB metal which was affected by postweld heat with increasing welding cycles showed that the enrichment in austenite content could be achieved up to a volume fraction comparable with that of parent metal. It is well known that the excellent corrosion behavior achievable in ASS is due to a controlled partitioning of alloying elements between the ferrite phase and the austenite phase. In wrought alloys, element distribution under quasi-equilibrium condition is achieved during solution annealing at high temperature before water quenching. The rapid cooling rate does not induce significant modifications in phase volume fraction and element partition between phases. In welding process, the thermal cycles are more complex and limited degrees of freedom are left to optimize the metal structure. In the present work, the analysis of the weld microstructures and the partition coefficients indicated that austenite phase and a limited amount of ferrite phase are located at austenite grain boundaries. In hybrid welds, the arc can preheat workpiece surface before laser irradiation and form a shallow-melting zone which reduces the reflectivity of workpiece for the laser. Consequently, the weld energy is increased. Especially in hybrid multipass welding process, the postweld heat is increased with increase of welding cycles. After the postweld thermal cycles, the distribution of ferrite-stabilizing and austenite-stabilizing elements in a subsurfacial region (3 mm from the top of the WB surface) became more pronounced and the calculated partition coefficients reached values comparable to those of cast solution treated AAS. This observation of the satisfactory phase distribution revealed from micrographs (in Fig. 4, 6, and 7), represents a promising result that will be validated by corrosion test to be presented in a future article.

The modification of the partition coefficients as a function of position from weld surface (in Fig. 8) is revealed to be of particular significance, the extent of microstructural and

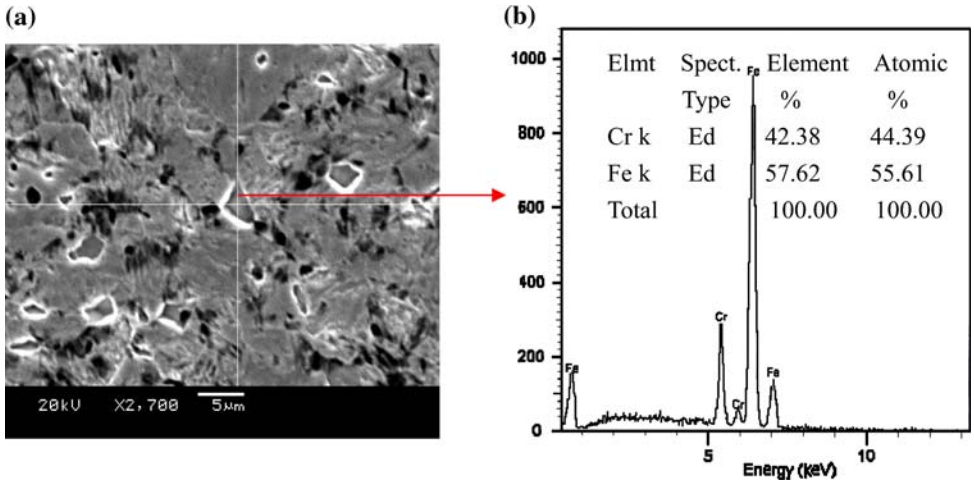

Fig. 9 The secondary electron image and EDS analysis of precipitated phase in WB. (a) Secondary electron image. (b) EDS analysis

chemical modification produced was investigated, and a good service behavior of the welded joint would be expected.

5. Conclusions

The low-power YAG laser-MAG arc hybrid multipass welding was carried out on an ASS workpiece. The microstructure features, phase composition, postweld heat influence, and WB precipitated phase were systematically analyzed. The results can be summarized as follows. The sound welds featured a narrow and regular weld metal zone without any solidification and shrinkage defects, and the successful joint of top and the bottom portions of the workpieces could be obtained by the optimized low-power YAG-MAG hybrid multipass welding process. The microstructures of different regions in WB are different, and the whole WB microstructures are composed of columnar γ-austenite and limited δ-ferrite phase, mainly located at grain boundaries. The fraction and morphology of δ-ferrite changed with increasing welding cycles, the fraction of δ-ferrite decreased from 20% to 10%, and its morphology changed orderly from lath, skeleton, vermicular to reticular. An accurate analysis of element partitioning between the two main phases was performed. It was shown the weld metal phase chemistry at 3 mm from the top of the WB surface underwent a notable modification that corresponded to an evolution of the partition coefficients toward the parent metal values due to the influence of postweld heat in hybrid multipass welding process. This indicated that the corrosion resistance of the microstructures would be equivalent to that of parent metal. The solidification of the weld metal was a nonequilibrium process and the quickest cooling rate in the root region of WB caused the σ phase to appear in the root region of WB. By analysis of microstructures and phase chemistry of WB, an effective welded microstructure that was close to WB surface could be obtained. These figures should be considered as reference parameters for the design of hybrid multipass welding of ASS steel structures.

Acknowledgment

This work was supported by the National Natural Science Foundation of China (No. 50675028).

References

1. W.M. Steen and M. Eboo, Arc Augmented Laser Welding, *Metal Constr.*, 1979, **11**(6), p 332–333, 335
2. H. Staufer, High Productivity by Using Laser-GMAW- and Laser-Tandem-Hybrid-processes for Thick Plates, *Weld. World*, 2005, **49**(9), p 66–74
3. R.P. Walduck and J. Biffin, Plasma Arc Augmented Laser Welding, *Weld. Metal Fabricat.*, 1994, **62**(4), p 172–176
4. U. Dilthey and H. Keller, Prospects in Laser-GMA Hybrid Welding of Steel, *Proceedings of the First International WLT-Conference on Lasers in Manufacturing*, Munich, 2001, p 453–465
5. M. El Rayes, C. Walz, and G. Sepold., The Influence of Various Hybrid Welding Parameters on Bead Geometry, *Weld. J.*, 2004, **83**(5), p 147–153
6. S. Kaierle, K. Bongard, M. Dahmen, and R. Poprawe, Innovative Hybrid Welding Process in an Industrial Application, *Proceedings of 19th International Congress on ICALE0 2000*, Section C-ICA-LEO 2000, p 91–98
7. T. Graf and H. Staufer, Laser-Hybrid Welding Drives VW Improvements, *Weld. J.*, 2003, **82**(1), p 42–48
8. U. Jasnau, J. Hoffmann, and P. Seyffarth. Nd:YAG-laser-GMA-Hybrid Welding in Shipbuilding and Steel Construction: "Robotic Welding," Intelligence and Automation, *LNCIS*, **299**, 2004, p 14–24
9. B.W. Shinn, D.F. Farson, and P.E. Denney, Laser Stabilisation of Arc Cathode Spots in Titanium Welding, *Sci. Technol. Weld. Join.*, 2005, **10**(4), p 475–481
10. B. Hu and G. den Ouden, Synergetic Effects of Hybrid Laser/Arc Welding, *Sci. Technol. Weld. Join.*, 2005, **10**(4), p 427–431
11. L. Liu, X. Liu, and S. Liu, Microstructure of Laser-TIG Hybrid Welds of Dissimilar Mg Alloy and Al Alloy with Ce as Interlayer, *Scripta Mater. J.*, 2006, **55**(4), p 383–386
12. G. Song, L. Liu, and P.C. Wang, Overlap Welding of Magnesium AZ31B Sheets Using Laser-Arc Hybrid Process, *Mater. Sci. Eng. A.*, 2006, **429**(1–2), p 312–319
13. L. Liu, X. Hao, and G. Song, A New Laser-Arc Hybrid Welding Technique Based on Energy Conservation, *Mater. Trans. A*, 2006, **47**(6), p 1611–1614
14. S. Gang, L. Liming, and C. Mingsheng, Investigations on Laser-TIG Hybrid Welding of Magnesium Alloys, *Mater. Sci. Forum.*, 2005, **488–489**, p 371–375
15. L. Liu, J. Wang, and G. Song, Hybrid Laser-TIG Welding, Laser Beam Welding and Gas Tungsten Arc Welding of AZ31B Magnesium Alloy, *Mater. Sci. Eng. A.*, 2004, **381**(1–2), p 129–133
16. L. Liu, X. Du, M. Zhu, and G. Chen, Research on the Microstructure and Properties of Weld Repairs in TA15 Titanium Alloy, *Mater. Sci. Eng. A.*, 2007, **445–446**, p 691–696
17. D. Hauser and J.E. Vanecho, Effects of Ferrite Content in Austenitic Stainless Steel Welds, *Weld. J.*, 1982, **61**(2), p 37–44
18. W.T. Delong, Ferrite in Austenitic Stainless Steel Weld Metal, *Weld. J.*, 1974, **53**(7), p 273–286

19. E.L. Hall and C.L. Briant, Chromium Depletion in the Vicinity of Carbides in Sensitized Austenitic Stainless Steels, *Metallurg. Trans. A.*, 1984, **15A**(5), p 793–811
20. E. Folkhard, X.Z. Li, and X.J. Zhu, *Stainless Welding Metallurgy.* Chemical Industrial Press, Beijing, 2004
21. J.C. Lippold and W.F. Savage, Solidification of Austenitic Stainless Steel Weldments-3. The Effect of Solidification Behavior on Hot Cracking Susceptibility, *Weld. J.*, 1982, **61**(12), p 388–396
22. J.A. Brooks, A.W. Thompson, and J.C. Williams, Fundamental Study of The Beneficial Effects of Delta Ferrite in Reducing Weld Cracking, *Weld. J.*, 1984, **63**(3), p 71–83
23. C.N. McCowan, T.A. Siewert, and D.L. Olson, Stainless Steel Weld Metal: Prediction of Ferrite Content, *WRC Bull.*, 1989, **342**, p 1–36
24. E. Capello, P. Chiarello, B. Previtali, and M. Vedani, Laser Welding and Surface Treatment of a 22Cr-5Ni-3Mo Duplex Stainless Steel, *Mater. Sci. Eng. A.*, 2003, **351**(1–2), p 334–343